

Cite this: DOI: 10.1039/xxxxxxxxxx

# Semi-automated on-demand control of individual droplets with a sample application to a drug screening assay<sup>†</sup>

Marie Hébert, Matthew Courtney, and Carolyn L. Ren<sup>a</sup>

Received Date

Accepted Date

DOI: 10.1039/xxxxxxxxxx

[www.rsc.org/journalname](http://www.rsc.org/journalname)

Automated control of individual droplets in microfluidic channels offers tremendous potential for applications requiring high accuracy and minimal user involvement. The feasibility of active droplet control has been previously demonstrated with pressure-driven flow control and visual feedback, but the manual operation required to perform droplet manipulations limited the accuracy, repeatability, and throughput. The present study improves upon the aforementioned challenges with a higher-level algorithm capturing the dynamics of droplet motion for a semi-automated control system. With a simple T-junction geometry, droplets can now be automatically and precisely controlled on-demand. Specifically, there is  $\pm 10\%$  accuracy for droplet generation,  $\pm 1.3\%$  monodispersity for 500  $\mu\text{m}$  long droplets and  $\pm 4\%$  accuracy for splitting ratios. On-demand merging, mixing, and sorting are also demonstrated as well as the application of a drug screening assay related to neurodegenerative disorders. Overall, this system serves as a foundation for a fully automated system that does not require valves, embedded electrodes, or complex multi-layer fabrication.

## 1 Introduction

Droplet microfluidics has been envisioned as an enabling technology for quantitative analysis using monodispersed picoliter- to nanoliter-sized droplets as reaction vesicles; they can be generated by injecting one fluid (i.e. water) into another immiscible fluid (i.e. oil) within a network of microchannels. Applications range across various fields including biological assays<sup>1,2</sup>, material synthesis<sup>3,4</sup>, water quality assessment<sup>5</sup> and many more. The key advantages of using droplet microfluidics lie in the low reagent consumption, shorter reaction time, and isolation of individual reactions from each other.

From a mechanical engineering perspective, the different needs of various applications can be simplified to a series of droplet manipulations performed in a desired order using droplet microfluidics as a platform. The manipulations include but are not limited to: generating, splitting, merging, trapping, mixing, and sorting droplets. The approaches to performing them can be categorized into passive or active methods. Notwithstanding the method selected, the challenge hindering most applications pertains to the

robust integration of the various functions on a unique platform.

### 1.1 Passive droplet manipulation

The extensive literature about passive droplet manipulations relies on the channel geometry and inherent physical properties of two-phase flow (e.g. interfacial tension)<sup>6</sup>. Manipulations such as generation<sup>7</sup>, splitting<sup>8,9</sup>, merging<sup>10</sup>, trapping<sup>11</sup>, and sorting<sup>12</sup> have been reported but with minimal integration of multiple functions sequentially on the same chip. Attempts at integrating multiple steps on a passive platform have been successfully achieved but incorporate only a limited number of functionalities<sup>13,14</sup>.

Although passive methods are widely used and studied, their robustness is challenged by manufacturing variations and defects, coupled dynamics, and operational uncertainties that require extensive experience in the microfluidic field to mitigate. Consequently, the passive microfluidic platforms are cumbersome to use for end-users in the biological or chemical engineering field for instance. Furthermore, the design of a microchannel network is application specific; thus, each change in the application (such as changes in droplet volumes or channel width) requires a revision of the design.

<sup>a</sup>Mechanical and Mechatronics Engineering at University of Waterloo, 200, University Avenue West, Waterloo, Ontario, Canada. Tel: +1 519 888 4567 x 33030; E-mail: c3ren@uwaterloo.ca

<sup>†</sup> Electronic Supplementary Information (ESI) available: S1 Software logic implementation, S2 Drug screening details, and videos of the automated manipulations: S3 generation, S4 double splitting, S5 merging, S6 mixing, and S7 fluorescent mixing. See DOI: 10.1039/b000000x/

## 1.2 Active droplet manipulation

In contrast to passive methods, active methods allow more control over droplets. While some methods focus on tuning the size of droplets generated passively for instance<sup>15,16</sup>, other techniques allow gaining control over individual droplets, for example, generating them on-demand<sup>17,18</sup>. Splitting has also been achieved through active methods such as those using magnetic force, but the platform deals with relatively large volume on the order of microliters<sup>19</sup>, or using surface acoustic waves (SAW), which requires more difficult manufacturing techniques for electrodes; although, Park *et al.* successfully demonstrated a reusable SAW substrate<sup>20</sup>. The ability to actively manipulate individual droplets is appealing to many applications, especially single particle or single cell analysis<sup>21</sup>. More control enables on-demand encapsulation of single cell or particle into individual droplets, removal of wastes after reactions by splitting droplets, perfusion of droplets with fresh media for continuous reactions by merging droplets, and long reaction time by trapping and storing droplets at the desired location. Such control can be achieved through the implementation of feedback control.

Controllers using feedback have been implemented in the context of microfluidics before to regulate: the size of the droplet generated<sup>22,23</sup>, droplet sorting<sup>24</sup>, hydrodynamic trapping<sup>25</sup>, and particle steering<sup>26</sup> amongst other applications. Nevertheless, direct control of droplets is more sparingly studied. Electrowetting-on-dielectric (EWOD) allows dispensing, mixing, and splitting<sup>27</sup>. The limitations associated with this platform include: direct contact between droplets and air making them susceptible to evaporation; potential cross-contamination from path crossing; relatively large droplet volume ill-suited for single-cell analysis due to the consequent low concentration; and limited applied voltage to prevent damage from the electric field to the biological compounds for certain applications<sup>28</sup>.

Active control of individual reaction vesicles has also been achieved using Quake's valves by controlling fluid flows in microchannel networks. This technique, however, requires more complex multilayer chip fabrication and bulky external equipment for the numerous solenoid valves<sup>29</sup>. Garstecki's group also used solenoid valves to generate droplets on-demand; the size of the input reagents can be independently tuned<sup>30,31</sup>. In their study, only one function (i.e. generation) is actively and precisely implemented while other functions such as merging rely on passive techniques. Improved control over multiple step processes such as dilution is achieved with high precision<sup>32</sup> as well as multiple manipulations<sup>33</sup>. However, the use of external valves is deemed more complicated and unnecessary with their fundamentally different approach. Hence, the approach with direct modulation of the inlet pressure (without additional hardware) is used.

## 1.3 Active control of individual droplet through pressure-driven flow using visual feedback

To ensure robust performance without compromising functionality, an ideal system should employ a simple channel network design and already-in-use hardware components to multiplex per-

formance. Such a proof-of-concept platform has been demonstrated using a simple T junction to perform an unrestrictedly long sequence of manipulations by leveraging the transparent properties of the chip materials with the quick pressure pump response. By using visual feedback to identify droplet location, the pressure can be adjusted to manipulate the droplets according to the user input as implemented in real-time using the computer mouse<sup>34</sup>. This strategy does not require complex multilayers, surface properties or electrode implementation. The geometry can be tuned to accommodate the specifications of a particular application; the number of inlets providing the different reagents can also be adjusted. In addition, the overall platform and principle can be reused without going through the lengthy design process and optimization typical of passive microfluidics.

Nonetheless, the caveat to the greater control is the loss of precision, speed, and repeatability of manipulations due to the lack of human operational accuracy. This becomes more challenging to end users with limited microfluidics experience. In order to increase the robustness and speed of the series of manipulations carried out to enable such a platform for practical applications, a higher-level of control is required so that users can set up their desired droplet manipulations via a graphic user interface (GUI) rather than manually moving a computer mouse. For example, users can set a specific droplet length to generate or a specific ratio the droplet should be split at by simply inputting these numbers in the GUI. The controller assisted with the camera visual feedback will take care of the rest. This automatic approach marks the beginning of the path leading to modular systems that can be widely adopted by end users.

The advancement from a manual movement of a computer mouse to such an automatic operation is very challenging. It requires: i) translation from intuitive human decisions to a sequential workflow that is executed by an algorithm implemented into the controller. For instance, an end user with minimal microfluidics experience can easily identify when two droplets have been successfully merged; however, translating this situation to a condition understood by the algorithm is not straightforward; and ii) the implementation of the logic must ensure a maximal robustness in order to minimize human interaction in case errors occur during the execution of the workflow. Considering merging of two droplets as an example, the workflow could stop operation when the identification of one droplet is momentarily unsuccessful due to image processing. This study aims to develop technologies to address these challenges towards the development of a fully automated platform that can be widely adopted for various applications and can be easily used without considerable microfluidics experience.

The end goal of a fully automated modular platform must be reached through stepping stones; the first one achieved was the manual control<sup>34</sup>; before the automated manipulations can be implemented, the semi-automatic procedure is an intermediate, yet large stepping stone. The functionalities developed with the semi-automatic manipulations will be at the core of the fully automated platform. In addition, the implementation of different semi-automatic manipulations is not trivial at all due to the complexity of translating the human thought process to a robust algo-

rithm. Succeeding the semi-automatic platform, the automated platform will integrate multiple semi-automatic manipulations as well as further intermediate functionalities such as moving a droplet across different channels. But most importantly, the automated platform will need to deal with the feasibility of the procedure. Hence, the semi-automatic mode is critical as a stepping stone considering that the fundamentals of the automated mode must be firmly established before moving on to the procedure logic. Finally, the modulated platform will need another algorithm layer to synchronize the modular automated platform modules between each other and with respect to the desired sequence.

## 2 Working principle

### 2.1 Manual control: modelling and controller design

The semi-automatic controller is built upon the controller developed for manual operation with the novelty lying in the largely eliminated human interaction during the procedure, and thus, the largely improved accuracy, repeatability and speed. All details concerning the basic modelling of the channel network and the design of the controller can be found in the previous study<sup>35</sup>. Briefly, manipulation of individual droplets in a channel network under pneumatic control is a complex dynamic system requiring the understanding of the dynamic coupling effects between the droplets, carrier fluid and applied pressures. The coupling effects are influenced by the channel geometry, interfacial tension, fluid properties and applied pressures, and governed by the mass conservation and law of motion. To model such a dynamic system for manipulation of individual droplets is very challenging involving coupled first- or higher-order differential equations. An alternative approach to the complex fluid mechanics equations is to develop a state-space model method through an analogy between the fluid system and an electrical circuit where: pressure is analogous to potential and velocity to current. A state-space model is a convenient matrix representation of first-order differential equations describing a physical system (including the coupled relationships) that leverages linear algebra for controller design.

The state of the dynamical system is fully represented by the state variable vector that includes: channel and tubing current (velocity), voltage (pressure) at the interface between channels and tubing, and voltage (pressure) at the chip junction where all three channels meet. Each channel within the network has an associated resistance (Equation 1), inductance (Equation 2), and capacitance (Equation 3) corresponding to viscous, inertia and compliance effects respectively.

$$R = \frac{32\mu l}{d_h^2} \quad (1)$$

where  $\mu$  is the dynamic viscosity [ $kg/m \cdot s$ ],  $l$  is the channel length [ $m$ ], and  $d_h$  is the hydraulic diameter [ $m$ ]

$$L = \rho l \quad (2)$$

where  $\rho$  is density [ $kg/m^3$ ] and  $l$  is channel length [ $m$ ]

$$C = \frac{A}{\kappa} + \frac{l}{\beta} \quad (3)$$

where  $A$  is the cross sectional area [ $m^2$ ],  $\kappa$  is the substrate stiffness [ $Pa \cdot m$ ],  $l$  is the channel length [ $m$ ], and  $\beta$  is the adiabatic bulk modulus [ $Pa$ ].

The interaction and coupling between the channels can be modelled by assembling the different individual *RLC* channel elements into a network. The state-space model is obtained through *Simulink* analysis with the standard format  $\dot{x} = Ax + Bu$ ,  $y = Cx$  where  $A, B, C$  completely characterizes the channel network configuration but also its dimensions and fluids used.

From the state-space model, a Linear Quadratic Regulator (LQR) controller with integral state feedback, and Kalman filter disturbance estimation and cancellation is designed as per<sup>35</sup>. The LQR is used to stabilize the unstable system; the integral of the states allow for zero steady error; the Kalman filter cancels the offset due to the Laplace pressure and other disturbances.

The inputs to the controller are the pressure applied at each of the inlets while its outputs are the displacement within each channel. The output is compared to a reference value for which the error asymptotically reaches zero through the controller.

### 2.2 Semi-automatic droplet control

#### 2.2.1 Fundamental functionality

The user can request droplet motion to the controller (e.g. adjusting the length of the droplet to be generated) by pulling the interface in so-called manual mode; however, precision, repeatability and speed vary between different manipulations of the same user, and from one user to the other. In this semi-automatic mode, the higher-level demands are inputted at the beginning through the GUI; leaving the rest to the algorithm and the controller.

The building blocks of the semi-automatic procedures are the measure, wait and move functions.

**Measure** The implementation of a relatively large feature with a nominal size of  $500 \mu m$  next to all channel network designs allows users to scale pixels to actual lengths. Image processing yields markers that indicate the interface between the continuous (carrier fluid) and dispersed (drop) phase. The distance between markers or from a marker to a junction can be measured using the calibration with the scaling factor.

The accuracy of such measurements depends on the resolution of the camera, the magnification of the microscope objective, and the calibration obtained from the  $500 \mu m$  feature. The typical resolution for the experiments carried with the 4X objective is  $3.302 \pm 0.007 \mu m/pixel$  (95%).

**Wait** The wait procedure is first initialized by resetting all internal variables, and setting the desired time delay as requested by the user input. Then, once the timer is started, the elapsed time is periodically compared to the desired delay. As long as the timer is smaller than the delay, the change in reference for the specified channel is set to 0, meaning that the droplet remains at the same position. Once the timer exceeds the delay, the procedure can move on to the next step or standby for further manipulations.

The comparison of the timer occurs at each loop of the software. The rate is dictated by the hardware and response time. The current system samples at 10 Hz and consequently, the accu-

racy is limited to  $\pm 0.1$  s.

**Move** Moving can be achieved either relative to the current position or to an absolute distance from the junction. The difference in implementation is only in setting the target position as the first step of the manoeuvre. Then, a proportional controller is applied and is characterized by a gain ( $K_{gain}$ ) and tolerance ( $\epsilon$ ). The gain represents the speed of moving the interface and the tolerance describes the acceptable difference between the objective ( $y_{objective}$ ) and current position ( $y_{current}$ ). The reference for the specified channel is then changed ( $dr$ ) until meeting the tolerance ( $\epsilon$ ). Note that the tolerance should be larger than the precision provided per pixel. A more complex controller is not implemented here considering that the change in reference is handled by a LQR controller with integral state feedback that already eliminates steady state error for tracking purposes.

$$dr = K_{gain}(y_{objective} - y_{current}) \quad (4)$$

The accuracy achieved is related to the calibration of micron per pixel that sets the lower limit. Nonetheless, due to the dynamic changes of the system and the limited actuating (i.e. pressure) power available, the achieved accuracy is generally larger than the calibration value.

### 2.2.2 Software implementation

The details of the logic behind the software implementation are included in ESI.S1<sup>†</sup> for the generation, merging and splitting of droplets with brief descriptions of every step.

The logic of the semi-automatic controller mimics the steps a user would perform in manual mode. Every step is performed as per the flowchart, for instance, for merging two droplets as shown in Figure 1. Each block type is defined in the legend as: user input, condition, semi-automatic control or data. The nomenclature concerning the chip itself is defined in the top right corner of the figure. The channels are arbitrarily separated at the junction. The interface between the water and oil phase is indicated for both the source channel (one interface) and a droplet (two interfaces, one at each end). The position of the interface can be defined from the junction point as the current position  $y$ . The image processing identifies the interface from the contrast between the two phases.

## 3 Experimental setup and methods

### 3.1 Materials and chip fabrication

The continuous phase used throughout all experiment is silicone oil with a viscosity of 50cst while ultrapure water is used as the dispersed phase unless otherwise indicated. If other fluids are required such as water-glycerol mixtures and oils of different viscosity, the changes in physical properties are reflected in the controller design<sup>35</sup>. Note that no surfactant is used for any of the experiments as the focus of this study is to develop a semi-automatic platform. Adding surfactants would change the interfacial tension which could be considered in the controller later.

The master of the microchannel network design is manufactured using a silicone wafer for its low surface roughness properties. SU-2025 (MICROCHEM) is spin coated in order to obtain a thickness of 50  $\mu\text{m}$  after which it is exposed to UV light through

the photomask. Then, the unexposed region is developed using SU8 developer. The chip is fabricated using polydimethylsiloxane (PDMS) and a standard soft-lithography procedure<sup>36</sup>.

### 3.2 System overview

The microfluidic chip manufactured as per section 3.1 is central to the system that is composed of four other components: camera, microscope, computer, and pressure pump shown in Figure 2. The arrows represent the flow of information. The time required to complete the loop is of crucial importance to the system stability. The current setup allows sampling at 10 Hz which is mainly limited by the pressure pump.

Visual feedback is provided by the camera and microscope, and is used to image the chip in real-time. Note that for this system, the field of view must be stationary and cannot be modified. Consequently, the microscope objective magnification is a trade-off between the size of the field of view and resolution (micron per pixel); the magnification used is 4X. The image is relayed to the computer through USB 3.0 communication and analyzed using image processing to extract the location of the two-phase interface. Then, the controller calculates the necessary actuation based on the current and desired positions. Finally, the pressure pump is instructed to apply the various pressure independently to each inlet of the chip.

## 4 Result and discussion

### 4.1 Automated on-demand individual manipulations

Each manipulation can be executed in an arbitrary order according to the desired application. Furthermore, if the results such as droplet length or splitting ratio are deemed unsatisfactory, the procedure can be repeated. The high versatility and multiplexing are key characteristics of this technique.

#### 4.1.1 Generation

Generating a droplet on-demand can be achieved through four main stages: filling the source channel, droplet adjustment in the destination channel, sectioning at the desired length with respect to the T junction, and stabilization. The performance achieved is  $\pm 10\%$  on the resulting droplet length for the requested droplet length ranging from 150 - 750  $\mu\text{m}$  as shown in Figure 3. The accuracy improves to  $\pm 5\%$  for longer requested droplet length because of the relatively smaller errors and the more stable junction region. The uncertainties are related to the resolution (micrometres per pixel) and the dynamic pressure variations (See Section 4.2.1 for more details). A smaller channel width of 50  $\mu\text{m}$  as compared to 100  $\mu\text{m}$  allows more robust generation of smaller droplets in the squeezing regime.

Furthermore, the monodispersity of the generated droplets is assessed through the standard deviation of a sample size of 43 for which a droplet length of 500  $\mu\text{m}$  was requested in a 50  $\mu\text{m}$  wide channel (see Table 1). The resulting monodispersity of the generated droplets (i.e. standard deviation divided by mean:  $\sigma/\bar{x}$ ) is 1.3%. Comparatively, monodispersity of droplets generated passively at a T junction has been reported as 2%<sup>37</sup>. The sequence of steps to generate a droplet is shown in Figure 4 as well as in

ESI.S3<sup>†</sup>.

**Table 1** Statistical analysis for droplet generation performance.

Description	Value
Requested length [ $\mu\text{m}$ ]	500
Sample mean $\bar{x}$ [ $\mu\text{m}$ ]	490
Sample standard deviation $\sigma$ [ $\mu\text{m}$ ]	6.5
Sample size	43
<b>Monodispersity (<math>\sigma/\mu</math>)</b>	<b>1.3 %</b>

#### 4.1.2 Splitting

The ratio at which a droplet is split into two daughter droplets can be selected with an accuracy of  $\pm 4\%$ . The droplet must first be manually positioned overlapping the two side channels across a T junction. Then, the distance from one end of the droplet to the junction is adjusted automatically before sectioning and stabilizing the two daughter droplets. The limitation of the smallest splitting ratio depends on the channel width ( $w$ ); a droplet of less than  $\sim 1.5w$  cannot be requested in order to stay within the squeezing regime as shown in Figure 5.

The control over individual droplet movement allows one of the daughter droplets from a first split to be moved to a section with a smaller channel width in order to split a second time. Hence, higher precision can be achieved if, for instance, the original droplet would be too large to fit within the field of view at the smaller width due to its consequent increased length. The control over the splitting procedure is foreseen to have potential in applications requiring a wash operation. The sequence of steps to successively split a droplet is shown in Figure 6 as well as in ESI.S4<sup>†</sup>.

#### 4.1.3 Merging

Merging of two droplets can be achieved by ensuring that the droplets, especially those of uneven length, reach the T junction simultaneously and with enough momentum to break their interface. The sequence of steps to merge two droplets is shown in Figure 7 as well as in ESI.S5<sup>†</sup>.

#### 4.1.4 Mixing

When two droplets containing different content are merged, mixing can be enhanced through active motion. Mixing in the droplet microfluidic context is challenging due to the inherent laminar nature of the flow. However, the T junction allows motion perpendicular to the two main vortices flowing symmetrically along the channel axis in a droplet. Hence, cross-flow is induced and significantly enhances mixing.

Mixing is quantified using the mixing index as defined by Danckwerts<sup>38</sup> where  $\langle \rangle$  denotes an average over all pixel values within the droplet boundary.

$$MI = 1 - \frac{\langle (N - \langle N \rangle)^2 \rangle}{\langle N \rangle (N_{max} - \langle N \rangle)} \quad (5)$$

In Figure 8, a mixing index threshold of 0.85 is deemed satisfactory. Moreover, the mixing index before merging considers the pixel values of both the water and dye droplets and is initially

low. Hence, the large increase of the mixing index shows the successful mixing through active control of the droplet. The active mixing is completed under 30 seconds. The manipulations could be improved and performed faster through higher actuation gains (although at the expense of stability) and automated steps.

The sequence of steps to mix two droplets is shown in Figure 9 as well as in ESI.S6<sup>†</sup>. Note that Figure 9 uses methylene blue dye to show the contrast between the two droplets while 100  $\mu\text{M}$  Thioflavine S fluorescent dye was used to gather the data for mixing index calculations during separate experiments.

#### 4.1.5 Sorting

Sorting can be implemented by discarding the undesirable droplet. When performing manipulations on a droplet, an unwanted daughter droplet of a split, for instance, can be moved in a continuous phase channel and discarded while the droplet of interest is retained and can be further processed.

The sorting capability is shown during the double splitting procedure in Figure 6; after the first split, one of the two daughter droplets is selected as desired for the second split procedure while the other is discarded hence effectively sorting the droplets.

The ability to arbitrarily select desired droplets is of particular interests for example following the result of an assay. Depending on the result, the droplet can be further processed or discarded. Furthermore, the combination with the immobilization capabilities is promising for applications requiring incubation.

## 4.2 Limitations and uncertainties

### 4.2.1 Generation and splitting precision

The limitations in terms of performance are determined by the width of the channel. Smaller channel width permits the generation and splitting into shorter length droplets.

The accuracy of generating and splitting droplets is established as  $\pm 10\%$  and  $\pm 4\%$  respectively; one of the limiting factors is the resolution of microns per pixel determined by the camera specifications. However, the main source of uncertainties is from the dynamic pressure changes. The main sources of short-term pressure oscillations are: the response of the pressure pump, PDMS compliance, and the sampling period. The most effective mitigation would be to improve the pressure actuation rate (currently, 10 Hz) because, within these 100 ms intervals, the pressure cannot be changed. Hence, the sampling rate represents a hard limit on the reduction of the short-term oscillations. Considering the current system, the two most significant delays limiting the sampling rate are the pump communication and image processing.

### 4.2.2 Throughput

One important drawback of this technique is the limited throughput that is traded off for the increased control on droplet manipulations. The currently limited sampling of 10 Hz for the hardware is a hard limit on the throughput. Furthermore, the manual manipulations currently required between the semi-automatic manipulations result in a throughput that cannot be pertinently calculated in Hertz. Nonetheless, the potential to fully automate the sequence of manipulations is foreseen to significantly improve the throughput compared to the semi-automatic mode.

## 5 Application to a drug screening assay

### 5.1 Context and motivation

Neurodegenerative disorders (e.g. Alzheimer's disease, Parkinson's disease) can be related to tau-protein aggregation<sup>39</sup>. The assay used herein aims to quantify the efficacy of an inhibitor (Orange G) in the presence of a peptide (Ac-VQIVYK-NH<sub>2</sub> (AcPHF6)), which is derived from a full-length tau protein. To quantify the aggregation, a fluorescent indicator dye (Thioflavine T (ThT)) is used<sup>40</sup>. The aggregation is triggered by the PBS buffer upon merging of the droplets: droplet A contains the peptide dissolved in ultrapure water while droplet B contains the fluorescent indicator with the inhibitor dissolved in buffer. The excitation and emission peaks of the fluorescent dye (ThT) shift upon physically binding the tau-aggregate, and therefore it can be used to track aggregation over time.

Microfluidics approaches to drug screening<sup>41</sup> have two main advantages over traditional 96-well plate assays<sup>42</sup>: reduced reaction time from the smaller length scales, and also, a lower cost associated with the reduced consumption of the expensive reagents.

### 5.2 Methodology

The following chemicals were obtained from *Sigma-Aldrich*: Orange G (for NA electrophoresis), Thioflavine T, solid Phosphate-buffered saline (PBS), and dimethyl sulfoxide (DMSO). The AcPHF6 peptide was acquired from *Celtek Peptides*. The DMSO was used to help dissolve the Orange G in the PBS buffer solution.

The microscope camera is used to record the fluorescent images (16-bit depth) and the data is extracted using post-image processing. The camera (Andor Zyla 5.5 sCMOS) is set to an exposure time of 2 seconds. The excitation wavelength is 440 nm while the emission wavelength is 490 nm using a fluorescence filter (CFP-HQ) with the inverted microscope (Nikon Ti-E).

While the fluorescent data is recorded for a period of more than 6 min (every 2 seconds) after merging of droplet A and B, the controller must be turned off because it is only operational for bright field view. Although the droplets mainly remain stationary, there can be slight movement along the channel. In order to track the droplet motion, a correlation along the channel is used with a mask of the droplet shape. Assuming that the background is dark (pixel value near 0), the fluorescence from the droplet will be taken into account in order to locate the droplet. After the mask is applied at the proper position, the average of all pixels value is simply taken. Further details are included in ESI.S2-1<sup>†</sup>.

Whether the dye self-aggregates or not is verified by taking a fluorescent image of the droplets and confirming that there is no significant fluorescent intensity compared to the background before merging.

The concentration of each compound after droplet merging is presented in Table 2. The two droplets merged are, nominally, of equal length beforehand. Consequently, the solutions prepared are twice (i.e. 32  $\mu$ M) the concentration indicated in the table (i.e. 16  $\mu$ M after merging).

Three trials were performed for each droplet composition. The first and second data set are collected from the same chip, on the

same day for repeatability purposes. The third data set is from a different chip on a different day for reproducibility purposes. Figure 10 shows the average pixel intensity of the three data sets with the corresponding standard deviation.

The ThT fluorescent indicator photobleaches due to its photosensitivity. Consequently, the initial intensity of the merged droplet decreases over time. In order to compare the data between different trials, the intensity is offset from the initial value to only analyze the difference (or increase) in fluorescent intensity. A negative control is also used to help confirm that the dye does not self-aggregate or increase with intensity over time.

### 5.3 Results and discussion

The results for the positive and negative experiments are presented in Figure 10 along with the results using the aggregation inhibitor Orange G. Figure 11 shows the images of the fluorescent intensity at several time steps for all three cases.

If the dye self-aggregates, there will be a fluorescent signal unrelated to the protein aggregation. Therefore, it is important to verify. The negative control confirms that this is not the case, as there is no significant increase in intensity. Furthermore to the negative control, the images (both bright field and fluorescent view) captured before the droplets merging are used to confirm that the dye is not emitting a fluorescent signal before the aggregation is triggered for all cases.

The positive control does not involve the Orange G chemical. The peptide (AcPHF6) aggregation is triggered by the PBS buffer upon merging. The fluorescent dye (ThT) is used to track the reaction as the intensity increases over time. Eventually, a plateau is reached and sets the intensity baseline that is compared to the experiments involving the aggregation inhibitor (Orange G). For those experiments, the 32  $\mu$ M Orange G solution is added to the droplet containing buffer and fluorescent dye. Orange G reduces aggregation which can clearly be seen with the lower fluorescent plateau in Figures 10 and 11.

### 5.4 Challenges and further direction

As previously mentioned, neurodegenerative disorders are linked to protein aggregation. While the fluorescent dye allows the aggregation to be tracked, analyzing how the aggregation is impacted by the addition of other chemicals is useful to develop drugs. The platform is applied to this particular assay as a proof of concept rather than a thorough study of the influence of Orange G on AcPHF6 protein aggregation. Certain challenges were encountered and are addressed in this subsection.

As noted for certain figures, the intensity of the screenshots is uniformly artificially increased for better readability while retaining the same trend. The overall weak fluorescent signal is attributed to photobleaching of the Thioflavine T dye. The illumination of the dye occurs during the setup (after the filled tubes are connected) as well as on-chip from the microscope light. Considering the slow flow rates (even often immobilized solutions), the photobleaching effects are significant and should be mitigated to study the protein aggregation more thoroughly.

Another main challenge is that the surface properties of PDMS

**Table 2** Final concentration after droplet merging for each compound.

Experiment	AcPHF6 [mg/ml]	ThT [ $\mu$ M]	Orange G [ $\mu$ M]	PBS buffer [mM]	DMSO (% v/v)
Positive control	0.06	3.0	—	16.0	< 1 %
Orange G	0.06	3.0	16.0	16.0	< 1 %
Negative control	—	3.0	—	16.0	< 1 %

chips degrade over time, limiting the amount of data that can be collected per chip. Moreover, PDMS is porous and will absorb the dye, leading to an overall increase in background intensity over time.

The chemical solutions used are temperature sensitive; warmer temperatures promote self-aggregation. The peptides can self-aggregate (without the PBS buffer) that is highly undesirable. Although the dye self-aggregation is controlled for by the screenshots before merging and the negative control, this caused problems on other trials not herein included. The reservoir holder with the vials is kept in an ice bath to maintain a low temperature. However, the small dimensions of the tubing connecting to the chip as well as the small channel dimensions lead to a quick thermal exchange with the room temperature. Once again, similarly to photobleaching, this negative factor is exacerbated by the slow flows used with this platform.

Finally, the impact of droplet length on concentration should be more thoroughly analyzed to better quantify the variations. This is further discussed in ESI.S2–3<sup>†</sup>. Nevertheless, the use of the active control platform to perform drug screening assays has advantages albeit requiring further work to address the challenges mentioned above.

The trapping mechanism is leveraged (albeit not perfectly due to the necessity of fluorescent images), and as demonstrated in ESI.S2–1<sup>†</sup>, the small displacement can be compensated for. Passive methods, on the other hand, face many more challenges to trap droplets. The solutions are tailored to a particular droplet volume for instance and would require different designs for different droplet lengths.

Moreover, the active platform has the potential to perform multiple tests on the same chip by adding more inlets with the solution for the negative control, Orange G concentration, and positive control. The Orange G concentration could also be varied by using 2 droplets of different length ratios before proceeding with the other steps. Different inhibitors at different concentrations could also be combined, and then, tested in parallel that is very beneficial and highly desirable for high-throughput screening.

The development of a controller operational also during fluorescent imaging would be useful to limit the displacement of droplets consistently and automatically for more efficient testing.

## 6 Conclusion

The work performed by Wong *et al.* was a proof-of-concept study in demonstrating active control of individual droplets through the actuation of the pressures as per the information extracted from the visual feedback. The caveat to the additional control was the loss of precision due to poor human repeatability and performance. Hence, a higher-level algorithm is developed and imple-

mented to achieve automated droplet generation on-demand of varying size, droplet splitting at specific ratios, merging, mixing, and sorting. Repeatability and robustness are of particular importance to use this platform for applications. Furthermore, the implementation does not require complex manufacturing techniques and although multiple functions are implemented, the footprint of the chip remain small due to the multiplexed functionality of the T junction.

A further advantage to this active droplet manipulation is the reduction in reagent consumption. Comparatively, passive droplet microfluidics requires a setup and stabilization phase that significantly increases reagent consumption as droplets are processed but not fit to be analyzed yet.

A natural extension of this work would be to further develop the semi-automatic algorithm to a fully automated mode. A procedure would be customized by the end user with minimal interaction required as it is automatically executed and data is collected. Hence, the platform would be more accessible to people in the biological or material science field as a tool without requiring in-depth knowledge about droplet microfluidics.

The application of the active control technology to a drug screening assay successfully demonstrated the potential impact of this microfluidics tool in another field. The positive and negative control curves for the kinetics of the tau-protein aggregation were obtained alongside a concentration of inhibitor (Orange G). The results demonstrated qualitatively the reduction of fluorescent aggregation by the inhibitor.

## Acknowledgments

This work was carried out thanks to grants from NSERC and OCE provided to Prof. Carolyn Ren. Other funding includes NSERC CGS-D scholarship and the Nanofellowship from the Waterloo Institute for Nanotechnology (WIN).

Marie would like to acknowledge the previous work carried out by David Wong setting the foundation for the work presented here as well as Anna Nguyen for the help provided in the laboratory.

## References

- 1 B. Zheng, C. J. Gerdtts and R. F. Ismagilov, *Current opinion in structural biology*, 2005, **15**, 548–555.
- 2 A. A. S. Bhagat, H. Bow, H. W. Hou, S. J. Tan, J. Han and C. T. Lim, *Medical & biological engineering & computing*, 2010, **48**, 999–1014.
- 3 I. Shestopalov, J. D. Tice and R. F. Ismagilov, *Lab on a Chip*, 2004, **4**, 316–321.
- 4 R. Karnik, F. Gu, P. Basto, C. Cannizzaro, L. Dean, W. Kyei-Manu, R. Langer and O. C. Farokhzad, *Nano letters*, 2008, **8**, 2906–2912.

- 5 F. Lefevre, A. Chalifour, L. Yu, V. Chodavarapu, P. Juneau and R. Izquierdo, *Lab on a Chip*, 2012, **12**, 787–793.
- 6 C.-X. Zhao and A. P. Middleberg, *Chemical Engineering Science*, 2011, **66**, 1394–1411.
- 7 P. Garstecki, M. J. Fuerstman, H. A. Stone and G. M. Whitesides, *Lab on a Chip*, 2006, **6**, 437–446.
- 8 D. Link, S. L. Anna, D. Weitz and H. Stone, *Physical review letters*, 2004, **92**, 054503.
- 9 M. Hein, M. Moskopp and R. Seemann, *Lab on a Chip*, 2015, **15**, 2879–2886.
- 10 X. Niu, S. Gulati, J. B. Edel *et al.*, *Lab on a chip*, 2008, **8**, 1837–1841.
- 11 Y. Bai, X. He, D. Liu, S. N. Patil, D. Bratton, A. Huebner, F. Hollfelder, C. Abell and W. T. Huck, *Lab on a chip*, 2010, **10**, 1281–1285.
- 12 A. C. Hatch, A. Patel, N. R. Beer and A. P. Lee, *Lab on a Chip*, 2013, **13**, 1308–1315.
- 13 X. Chen and C. L. Ren, *RSC Advances*, 2017, **7**, 16738–16750.
- 14 L.-H. Hung, K. M. Choi, W.-Y. Tseng, Y.-C. Tan, K. J. Shea and A. P. Lee, *Lab on a Chip*, 2006, **6**, 174–178.
- 15 H. Kim, D. Luo, D. Link, D. A. Weitz, M. Marquez and Z. Cheng, *Applied Physics Letters*, 2007, **91**, 133106.
- 16 E. Castro-Hernández, P. García-Sánchez, S. H. Tan, A. M. Gañán-Calvo, J.-C. Baret and A. Ramos, *Microfluidics and Nanofluidics*, 2015, **19**, 787–794.
- 17 S.-Y. Park, T.-H. Wu, Y. Chen, M. A. Teitell and P.-Y. Chiou, *Lab on a Chip*, 2011, **11**, 1010–1012.
- 18 S. Kahkeshani and D. Di Carlo, *Lab on a Chip*, 2016, **16**, 2474–2480.
- 19 T. J. Hutama and R. D. Oleschuk, *Lab on a Chip*, 2017, **17**, 2640–2649.
- 20 J. Park, J. H. Jung, K. Park, G. Destgeer, H. Ahmed, R. Ahmad and H. J. Sung, *Lab on a Chip*, 2018, **18**, 422–432.
- 21 L. Armbrrecht and P. Dittrich, *Analytical Chemistry*, 2017, **89**, 2–21.
- 22 E. Miller, M. Rotea and J. P. Rothstein, *Lab on a Chip*, 2010, **10**, 1293–1301.
- 23 W. Zeng, S. Li and Z. Wang, *Sensors and Actuators A: Physical*, 2015, **233**, 542–547.
- 24 J. Maddala, B. Srinivasan, S. S. Bithi, S. A. Vanapalli and R. Rengaswamy, *AIChE Journal*, 2012, **58**, 2120–2130.
- 25 A. Shenoy, M. Tanyeri and C. M. Schroeder, *Microfluidics and Nanofluidics*, 2015, **18**, 1055–1066.
- 26 M. D. Armani, S. V. Chaudhary, R. Probst and B. Shapiro, *Journal of Microelectromechanical systems*, 2006, **15**, 945–956.
- 27 S.-K. Fan, C. Hashi and C.-J. Kim, *Micro Electro Mechanical Systems*, 2003. MEMS-03 Kyoto. IEEE the Sixteenth Annual International Conference on, 2003, pp. 694–697.
- 28 X. Xu, L. Sun, L. Chen, Z. Zhou, J. Xiao and Y. Zhang, *Biomechanics*, 2014, **8**, 064107.
- 29 T. Thorsen, S. J. Maerkl and S. R. Quake, *Science*, 2002, **298**, 580–584.
- 30 K. Churski, P. Korczyk and P. Garstecki, *Lab on a Chip*, 2010, **10**, 816–818.
- 31 K. Churski, T. S. Kaminski, S. Jakiela, W. Kamysz, W. Baranska-Rybak, D. B. Weibel and P. Garstecki, *Lab on a Chip*, 2012, **12**, 1629–1637.
- 32 W. Postek, T. Kaminski and P. Garstecki, *Analyst*, 2017, **142**, 2901–2911.
- 33 S. Jakiela, T. S. Kaminski, O. Cybulski, D. B. Weibel and P. Garstecki, *Angewandte Chemie International Edition*, 2013, **52**, 8908–8911.
- 34 D. Wong and C. L. Ren, *Lab on a Chip*, 2016, **16**, 3317–3329.
- 35 Y. H. Wong, *M.Sc. thesis*, University of Waterloo, 2016.
- 36 D. Qin, Y. Xia and G. M. Whitesides, *Nat.Protocols*, 2010, **5**, 491–502.
- 37 J. Xu, S. Li, J. Tan, Y. Wang and G. Luo, *AIChE journal*, 2006, **52**, 3005–3010.
- 38 P. Danckwerts, *Applied Scientific Research, Section A*, 1952, **3**, 279–296.
- 39 T. Mohamed, T. Hoang, M. Jelokhani-Niaraki and P. P. Rao, *ACS chemical neuroscience*, 2013, **4**, 1559–1570.
- 40 S. A. Sievers, J. Karanicolas, H. W. Chang, A. Zhao, L. Jiang, O. Zirafi, J. T. Stevens, J. Münch, D. Baker and D. Eisenberg, *Nature*, 2011, **475**, 96.
- 41 M. Courtney, X. Chen, S. Chan, T. Mohamed, P. P. Rao and C. L. Ren, *Analytical chemistry*, 2016, **89**, 910–915.
- 42 S. A. Hudson, H. Ecroyd, T. W. Kee and J. A. Carver, *The FEBS journal*, 2009, **276**, 5960–5972.

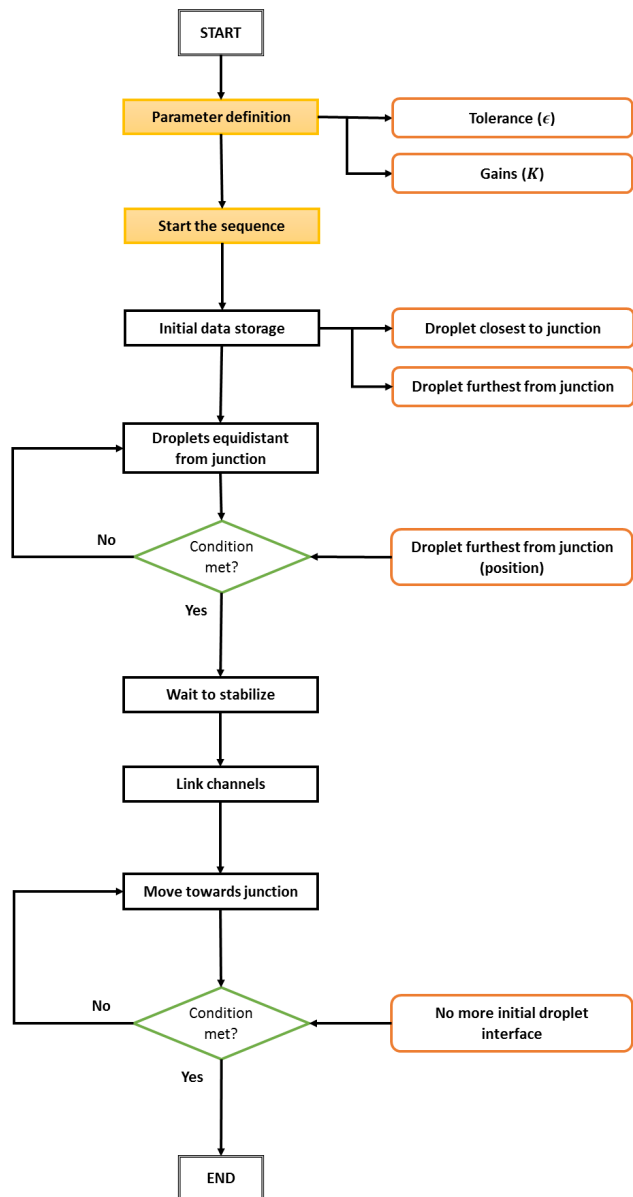
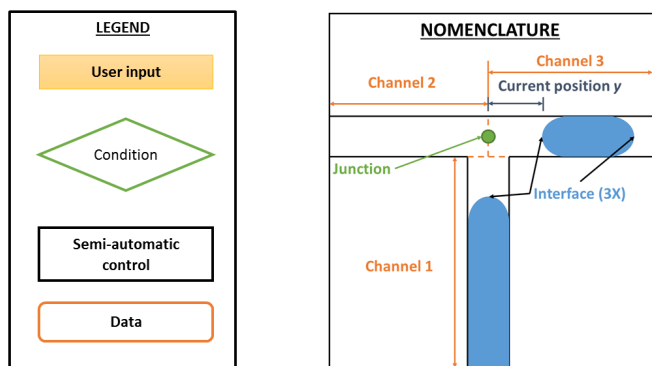


**Fig. 1** Flowchart representation of software logic for merging two droplets.

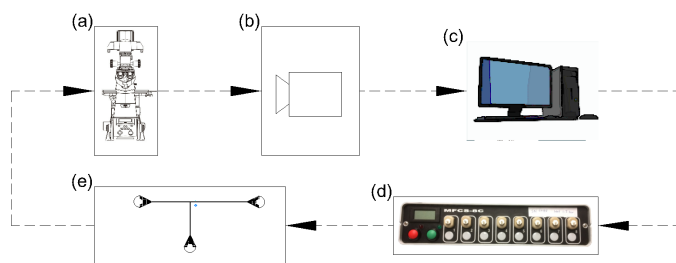


**Fig. 2** System overview for active control of droplet in microchannels through pressure-driven flow. (a) Nikon Inverted Microscope ECLIPSE Ti-E, (b) Andor Zyla 5.5 sCMOS camera, (c) personal computer, (d) Fluigent MFCS-8c pressure pump, (e) microfluidic chip.

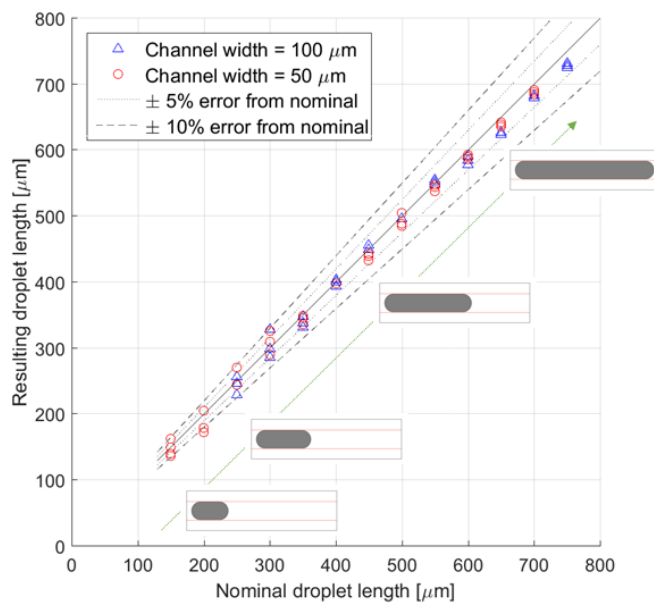


**Fig. 3** On-demand droplet generation distribution using semi-automatic control.

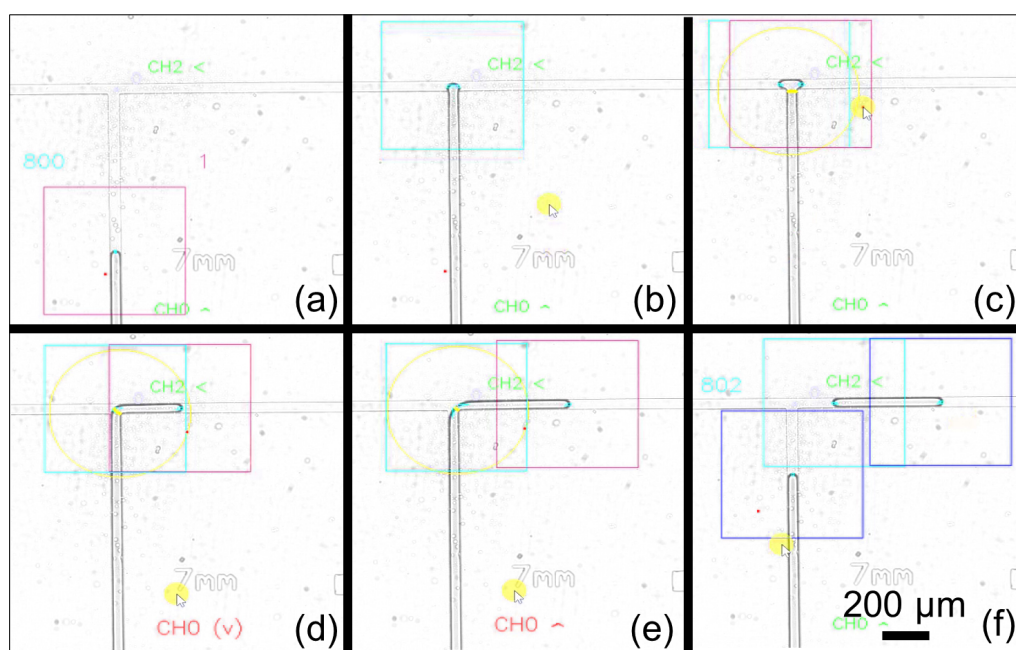


**Fig. 4** Droplet generation process (a) Source channel setup completed and ready to generate droplet (b) Filling of the source channel and overflow in other channels at the T junction (c) Manual selection of the new marker in the destination channel (d) Adjustment of the droplet length with respect to the junction (e) Droplet sectioning (f) Final stage with both interfaces stabilized.

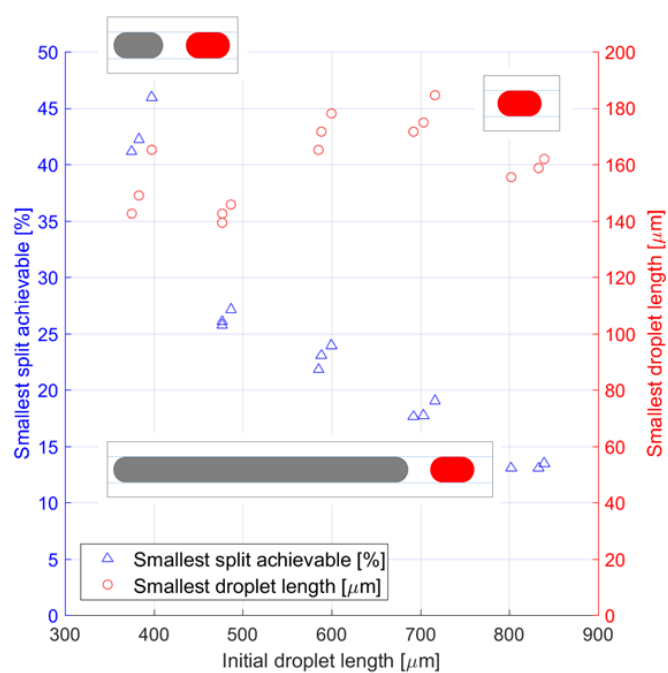


**Fig. 5** On-demand droplet splitting distribution using semi-automatic control.

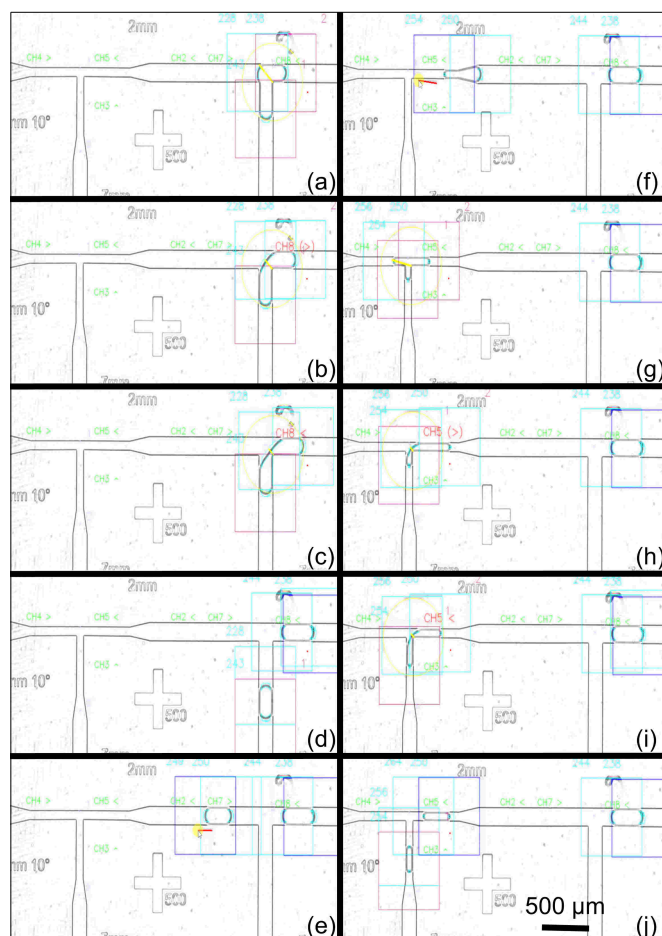


**Fig. 6** Successive droplet splitting process (a) Setup of the initial droplet (b) Adjusting the distance of markers with respect to the junction and the desired split ratio (c) Sectioning the droplet (d) First split completed for the 150  $\mu\text{m}$  channel width (e) Sorting of the desired droplet to be split again (f) Transition to the 75  $\mu\text{m}$  channel width region (g) Manual setup of the droplet (h) Adjusting the distance with respect to the second junction (i) Sectioning the daughter droplet (j) Final product of the double splitting with greater precision.

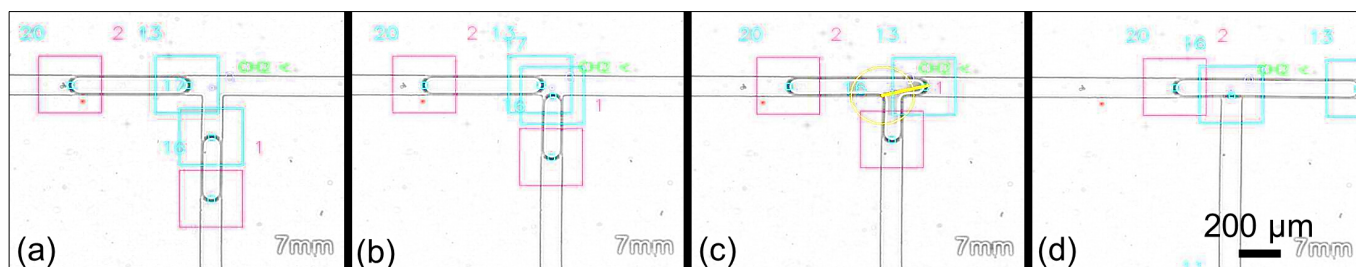


**Fig. 7** Droplet merging process (a) Initial manual setup of the two droplets on either side of the T junction (b) Both droplets reach the T junction simultaneously (c) The interface breaks and the two droplets merge (d) Merging is complete.

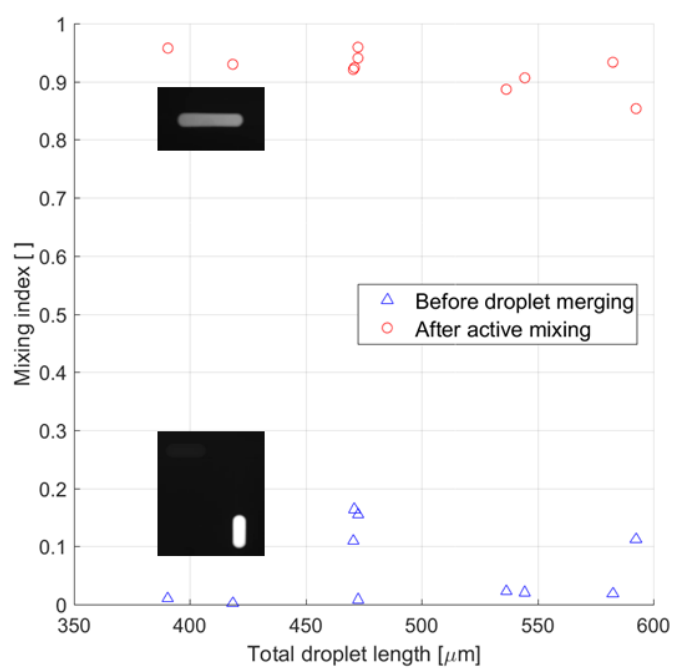


**Fig. 8** On-demand droplet mixing index according to resulting droplet total length.

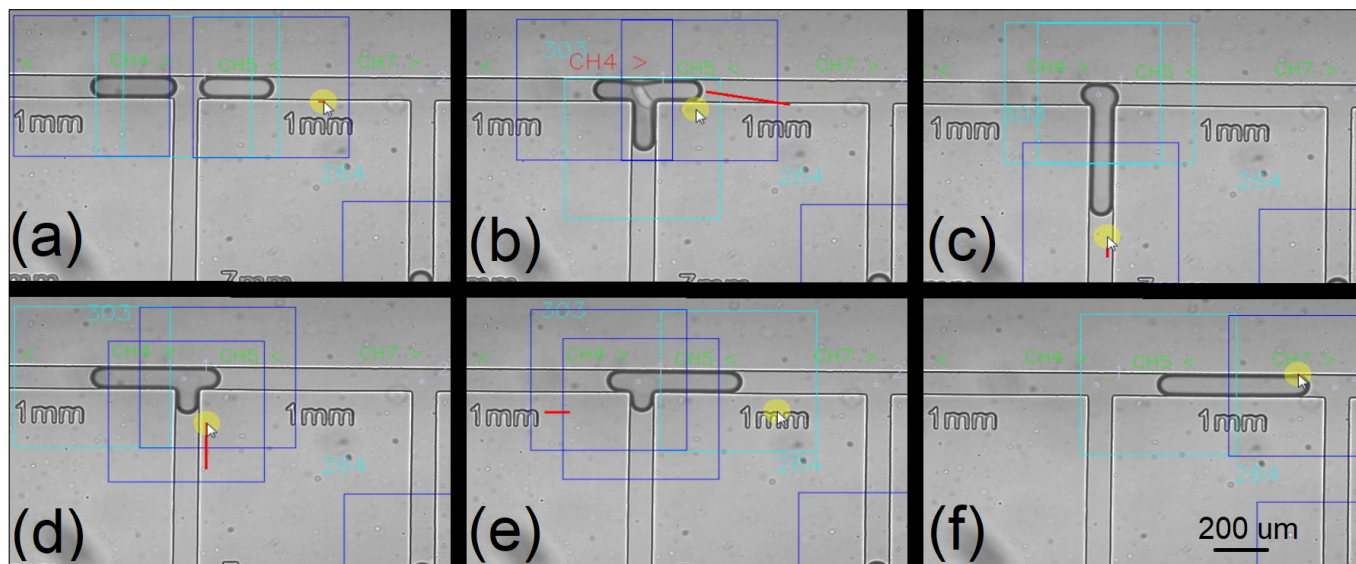


**Fig. 9** Droplet mixing process (a) Initial manual setup of the two droplets on either side of the T junction (b) Merging of the two droplets (c) Initial position after merging before mixing manipulations (d) Mixing on one side of the T junction with part of the droplet in each of the three channel (e) Transition to the destination channel with once again a part of the droplet in the third channel to break the symmetry of flow within the droplet (f) Final droplet fully mixed.

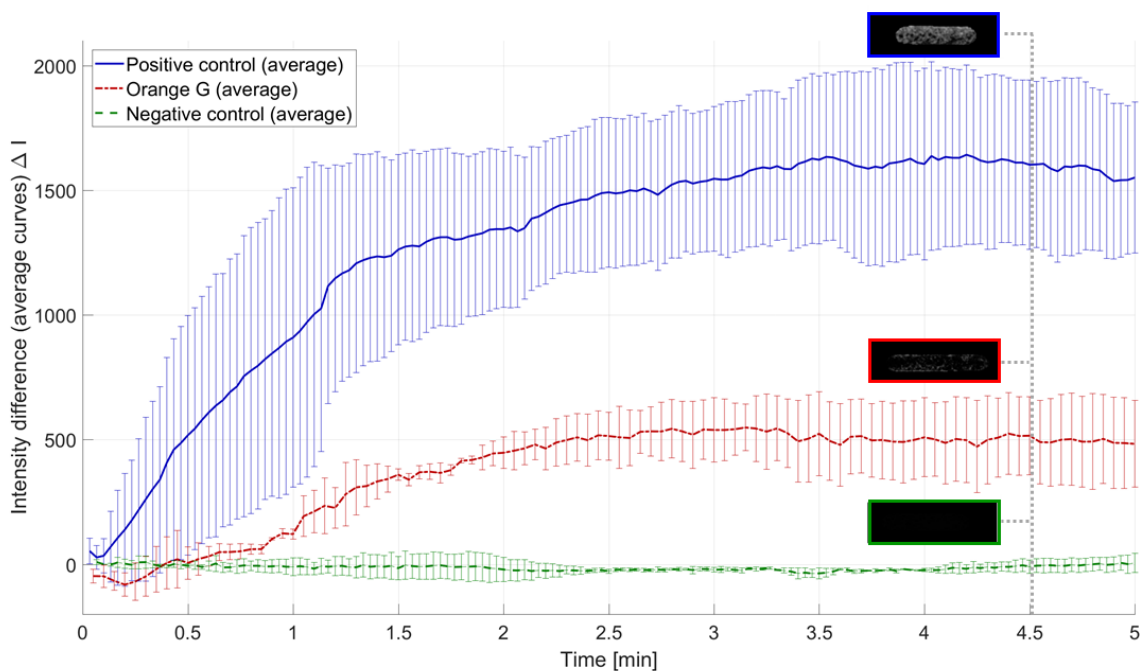


**Fig. 10** Fluorescent intensity change of Thioflavine T corresponding to the aggregation of AcPHF6 over time with and without the Orange G inhibitor. Error bars show standard deviation for 3 sets of experiments. Qualitative assessment showing the reduced fluorescent aggregation from the inhibitor.

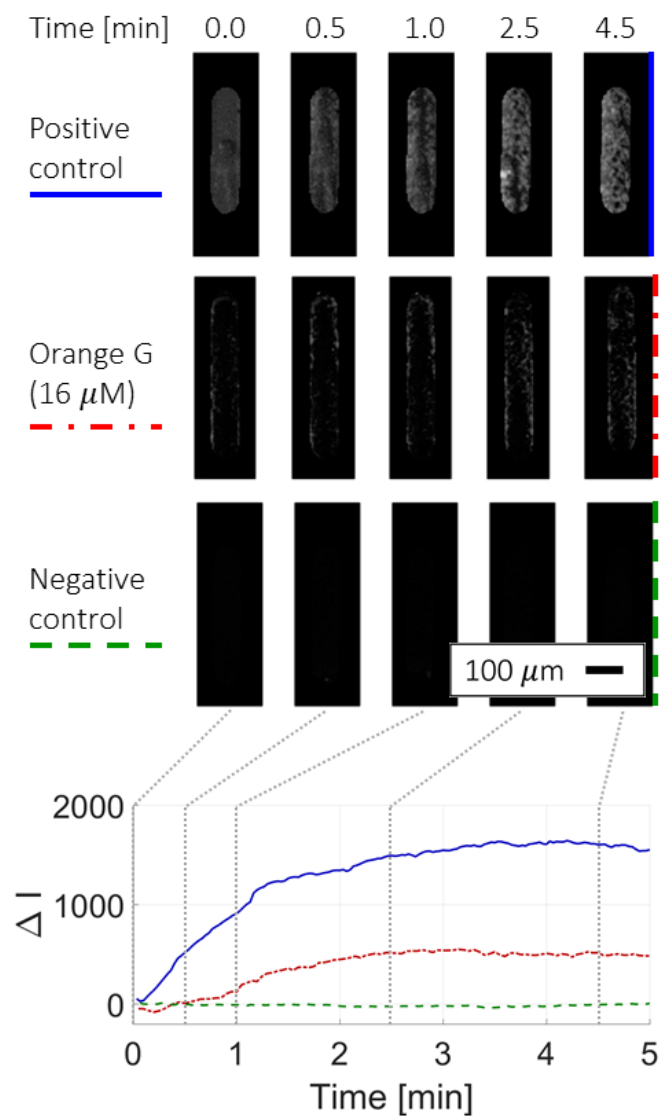


**Fig. 11** Artificially brighter screenshots of fluorescent intensity change of Thioflavine T corresponding to the aggregation of AcPHF6 over time with and without the Orange G inhibitor. Original image comparison shown in ESI.S2-2<sup>†</sup>.